AGU PUBLICATIONS

JGR

Journal of Geophysical Research: Atmospheres

RESEARCH ARTICLE
10.1002/2016JD024965

Key Points:
- Convection precursors on the globe are presented
- The key factors, convergence and CAPE, have different contribution in the convection
- Better estimation of convergence and CAPE is critical for accurate forecast of convection

Correspondence to:
Y. Miyamoto,
ymiyamoto@riken.jp

Citation:
Miyamoto, Y., T. Yamaura, R. Yoshida, H. Yashiro, H. Tomita, and Y. Kajikawa (2016), Precursors of deep moist convection in a subkilometer global simulation, *J. Geophys. Res. Atmos.*, *121*, 12,080–12,088, doi:10.1002/2016JD024965.

Received 18 FEB 2016
Accepted 26 SEP 2016
Accepted article online 28 SEP 2016
Published online 26 OCT 2016

Precursors of deep moist convection in a subkilometer global simulation

Yoshiaki Miyamoto[1,2], Tsuyoshi Yamaura[2], Ryuji Yoshida[2,3], Hisashi Yashiro[2], Hirofumi Tomita[2,4], and Yoshiyuki Kajikawa[2,3]

[1]Rosenstiel School of Marine and Atmospheric Science, University of Miami, Miami, Florida, USA, [2]RIKEN Advanced Institute for Computational Science, Kobe, Japan, [3]Research Center for Urban Safety and Security, Kobe University, Kobe, Japan, [4]Seamless Environmental Prediction Research, Japan Agency for Marine-Earth Science and Technology, Yokohama, Japan

Abstract Deep moist convection in the atmosphere plays an important role in cloudy weather disturbances, such as hurricanes, and even in the global climate. The convection often causes disastrous heavy rainfall, and predicting such convection is therefore critical for both disaster prevention and climate projection. Although the key parameters for convection have been pointed out, understanding the preprocesses of convection is a challenging issue. Here we identified the precursors of convection by analyzing a global simulated data set with very high resolution in time and space. We found that the mass convergence near the Earth's surface changed significantly several minutes *before* the initiation of early convection (the formation of cumulus clouds), which occurred with the increase in the convective available potential energy (CAPE). Decomposition of the statistical data revealed that a higher-CAPE environment resulted in stronger convection than in the stronger-convergence case. Furthermore, for the stronger-convergence case, the precursor was detected earlier than the total average (10–15 min before the initiation), whereas the amplitude of maximum velocity was not so strong as the higher-CAPE case. This suggests that the strength of convection is connected with CAPE, and the predictability is sensitive to the convergence.

1. Introduction

Different types of convection exist simultaneously in the global atmosphere. Deep moist convection develops vertically, extends through the entire troposphere, and is driven by buoyancy due to the phase changes of water [*Byers and Braham*, 1948a]. Convection plays an essential role in transferring momentum, energy, and chemical species in the atmosphere [*LeMone and Zipser*, 1980; *Ching and Alkezweeny*, 1986; *Jorgensen and LeMone*, 1989; *Takemi*, 2008; *Nasuno and Satoh*, 2011; *Masunaga and L'Ecuyer*, 2014] and affects general circulation [*Stevens and Bony*, 2013; *Bony et al*., 2015]. Furthermore, convection is the source of local torrential downpours that cause severe disasters. Along with understanding the mechanism of convection, one of the greatest challenges in current meteorological research is the accurate prediction of convection [*Doswell*, 1985; *Stevens and Bony*, 2013], i.e., when and where it will occur.

The driving mechanism of convection has been studied intensively under various conditions. Convection is created by thermodynamic and dynamic forces [*Emanuel*, 1994; *Houze*, 1994; *Jorgensen and Weckwerth*, 2003; *Weckwerth and Parsons*, 2006]. When the atmosphere is conditionally unstable, convection forms from a weak perturbed motion to make the atmosphere stable. On the other hand, convection can also be formed by a strong mass convergence in the boundary layer, which causes upward motion in the upper or above the top of the boundary layer. The vertical motion results in the condensation of water and acceleration of the vertical velocity. Once convection develops, it usually causes precipitation as a result of growing processes of water/ice droplets in convective clouds.

In general, convection has traditionally been understood as an atmospheric phenomenon with a high degree of randomness that can be predicted in advance at time scales only in the order of a few tens of minutes [*Lorenz*, 1969]. The temporal and spatial scales of convection are in the orders of 1 h to 1 km [*Byers and Braham*, 1948b; *Emanuel*, 1994; *Houze*, 1994], respectively, which are 2 to 3 orders of magnitude smaller than synoptic-scale or meso-alpha-scale systems and play important roles both in short- and long-range forecasts [*Zhang et al*., 2003; *Petch*, 2004; *Hohenegger and Schär*, 2007a, 2007b; *Zhang et al*., 2007; *Melhauser and Zhang*, 2012]. From the synoptic-scale or mesoscale perspective, this convection forms due to small-scale perturbations. Nonlinearity due to phase change processes also cause interference in

accurately predicting the mechanisms in large-scale systems that determine the environmental conditions of convection.

For accurate prediction, better understanding of preprocesses of convection is essentially needed. A number of studies have investigated the processes leading to convection, and it is understood that low-level mass convergence plays an important role in initiating deep convection [*Kalthoff et al*., 2009; *Barthlott et al*., 2010; *Behrendt et al*., 2011; *Birch et al*., 2014]. However, the main focus of many studies has been on large-scale convective systems [*Sherwood and Wahrlich*, 1999; *Mapes et al*., 2009; *Masunaga*, 2014; *Masunaga and L'Ecuyer*, 2014], while other studies have focused on convection in specific regions or under certain background conditions [*Wulfmeyer et al*., 2008; *Plant*, 2009; *Barthlott et al*., 2011; *Behrendt et al*., 2011; *Wulfmeyer et al*., 2011; *Birch et al*., 2014]. Because convection appears to be sensitive to its environmental conditions, it is expected to vary widely around the globe [*Miyamoto et al*., 2015].

This study was the first attempt to investigate the precursors of deep moist convection under various conditions in the Earth's atmosphere. We show the existence of precursors whose magnitude changed significantly before the initiation of moist convection based on a statistical analysis of the global simulation. The simulation was conducted with the extremely fine grid point spacing (0.87 km) that is finest possible with the computer resources available [*Miyamoto et al*., 2013, 2015; *Kajikawa et al*., 2016]. These high-resolution global simulation data provided tens of thousands of convection samples under a variety of cloud disturbances [*Miyamoto et al*., 2015].

2. Simulation Data and Definition of Cloudy Disturbances

We conducted a numerical simulation of a global atmosphere with subkilometer resolution using the Nonhydrostatic Icosahedral Atmospheric Model (NICAM) [*Tomita and Satoh*, 2004; *Satoh et al*., 2008, 2014]. The experimental settings were identical to those of *Miyamoto et al*. [2013]. The horizontal model resolution was 0.87 km, and the vertical resolution of 94 layers increased from 40 m at the bottom to 40 km at the top. The physical processes were solved by the following parameterizations: long-wave and short-wave radiation [*Sekiguchi and Nakajima*, 2009], cloud microphysics [*Tomita*, 2008], boundary layer turbulence [*Nakanishi and Niino*, 2004; *Noda et al*., 2010], and surface fluxes [*Louis*, 1979]. In the simulation, cumulus parameterization was omitted. The initial condition was built from a 3 day simulation result, with 3.5 km resolution. The initial condition for the 3 day integration was the linearly interpolated data at 2012082200UTC of the National Center for Atmospheric Research final analysis [*Kalnay et al*., 1996]. A 13 h simulation was conducted from 2012082500UTC, and the results from the final hour were used in this study. To examine the life cycle of the convection, the output interval was 1 min for a target period of 1 h from 2012082512UTC. Although the period for the analysis is much shorter than the time scale of environmental flow of convection, it is long enough to cover the lifetime of convection (a few tens of minutes), and a number of convection samples are detected over various regions on the globe as shown below.

The predictability of convection was statistically examined by considering the characteristics of the physical quantities *before* the initiation of convection. Hence, the life cycle of convection needed to be determined in the simulated result. In this study, we refer to the onset of the convection-forming stage as the initiation of convection (see below for the quantitative definition). We used the two-step methodology of *Miyamoto et al*. [2013] for detecting the convective grid points and the convection core. The convective grid points were defined as the grid points in which the vertically averaged total water and ice mixing ratios exceeded 0.2 g kg^{-3}. The vertical averages were estimated from the 1.5 km height to the tropopause height. The convection core grid points were then detected as local peaks of the vertically averaged vertical velocity. In this study, the vertically averaged water and ice mixing ratios were used to diagnose the convective grid points, rather than the cloud optical thickness and cloud top pressure as done by *Miyamoto et al*. [2013] to utilize the International Satellite Cloud Climatology Project (ISCCP) table [*Rossow and Schiffer*, 1999]. Furthermore, the troposphere was divided into five layers and the vertical averages were estimated for each layer. The convection core grid points were detected at each layer. This methodology was applied to each output time (every 1 min in this case). As a result, we obtained a data set of convection core grid points that contained information on the horizontal location, layer, and convection parameters, such as CAPE, at each output time.

We developed the following tracking algorithm for the convection core grid points. The core grid points were diagnosed to survive in the time interval from $t = t_1$ to $t_1 + \Delta t$, where Δt is the output interval. If there was a

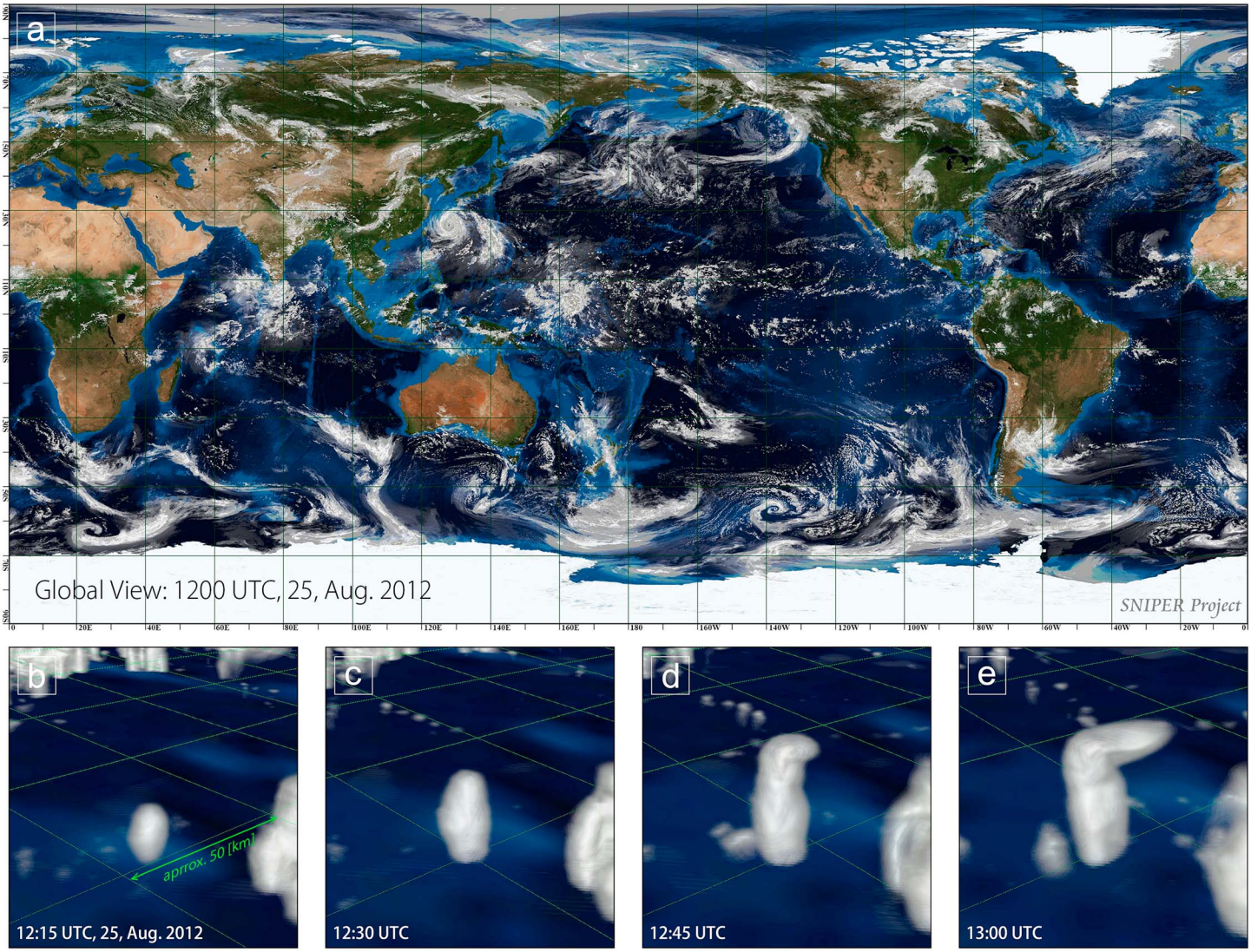

Figure 1. (a) Horizontal view of a simulated cloud field at 201208251200UTC and (b–e) a magnified view of a developing convective cell. The white color shows the mixing ratio of hydrometeors. The topography and bathymetry are from Blue Marble (August) by Reto Stöckli, NASA Earth Observatory.

core grid point at $t = t_1 + \Delta t$ within two-grid point distance (~1.74 km) from a core grid point at $t = t_1$, these two cores were considered identical. The searching process at $t = t_1 + \Delta t$ started from the core grid point at $t = t_1$; then, the four neighboring grid points were examined; and finally, the other grid points, apart from the grid point at $t = t_1$, were diagnosed. This seems to be a reasonable approach. Because the velocity to move a grid point distance (0.87 km) in 60 s (the output interval) is 14.5 m s^{-1}, the possibility of the existence of a convection core rarely exceeded this value after vertically averaging the horizontal velocity. The core grid points that were sustained for at least 10 min were detected as the convection grid points. Applying this methodology to the 1 h simulation data, we obtained more than 30,000 convection samples.

3. Results and Discussion

Figure 1a shows our simulated cloud field on the globe at 201208251200UTC. A variety of clouds and cloudy disturbances were simulated, and the simulation accurately captured the realistic cloud field [*Leinonen et al.*, 2015]. More detailed comparisons of the subkilometer simulation with observations can be found in *Kajikawa et al.* [2016]. Figures 1b–1e depict the typical life cycle of a cloud cell located at approximately (longitude, latitude) = (177, 0) at 15 min intervals. The cloud cell forms, or, more precisely, the

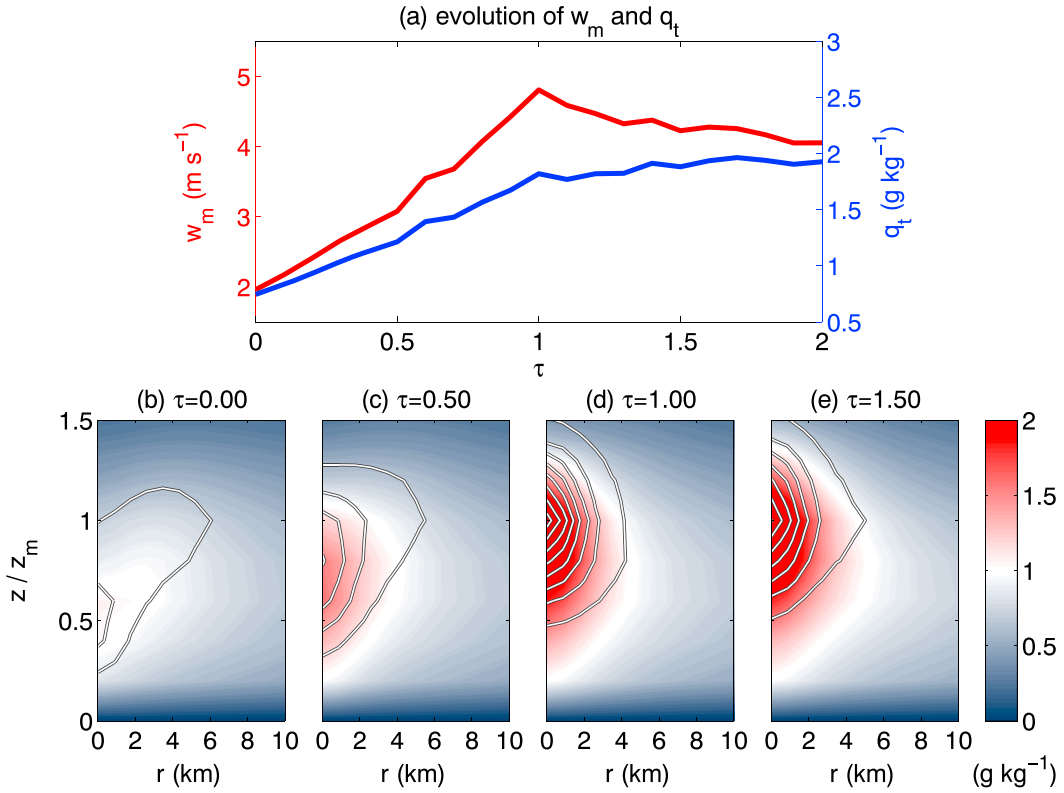

Figure 2. (a) Time series of maximum vertical velocity (the red line) and mixing ratio of water and ice at the core grid point of detected convection that is vertically averaged from $z = 1.5$ km to the tropopause altitude (the blue line). They are the arithmetic mean of all the detected convection samples. (b–e) Composite radius-height cross sections of total water-mixing ratio (shaded) and vertical velocity (contour). The contour interval is 0.5 m s^{-1}. The vertical axis is nondimensionalized by the altitude at which the vertical velocity reaches the lifetime maximum of each convection.

cloud water-mixing ratio becomes large enough to be drawn (approximately 0.2 g kg^{-1}). It grows vertically, and the vertical extent of the high water content region reaches a maximum in approximately 20 min. Then, an anvil forms at the top of the troposphere. The structural evolution, as well as its time scale, is consistent with the observed isolated thunderstorm [*Byers and Braham*, 1948b; *Emanuel*, 1994; *Houze*, 1994].

Applying the scheme to the simulation data, we obtained 30,100 convection samples throughout the globe over 1 h of simulation. To validate the developed method, we examine the temporal evolutions of parameters averaged by all the detected convection (Figure 2). The composites were constructed after the time is non-dimensionalized by that when the vertical velocity reaches the lifetime maximum of each convection ($\tau = 1$) to remove inconsistency of convection lifetimes. Figure 2a shows the time series of maximum vertical velocity and vertically averaged total hydrometeors. The maximum vertical velocity is initially small ($\tau = 0$, when the convection is first detected) and evolves until the peak time ($\tau = 1$). The vertically averaged total mixing ratio that is the sum of water and ice evolves in a similar way to the vertical velocity: it amplifies from a small value to the maximum at $\tau = 1$ when the vertical velocity reaches its lifetime maximum.

Figures 2b–2e show the composite radius-height cross sections of vertical velocity and total mixing ratios. It is indicated that the vertical velocity and cloud water are initially weak and concentrated in the lower troposphere. The peaks of both quantities raise up to higher altitudes with amplifying their magnitudes. When the vertical velocity reaches the maximum ($\tau = 1$), the peaks are located in the upper troposphere. Then, they decay afterward. The radial extents of large mixing ratio and vertical-velocity region are about 2–3 km. On average, the time at which the vertical velocity reaches its maximum after the first detection of convection (i.e., from $\tau = 0$ to 1) is about 10 min. Comparison of the composites (and some examples) with observational data indicates that the methodology of detecting the developed convection in this study is applicable to the global simulation data.

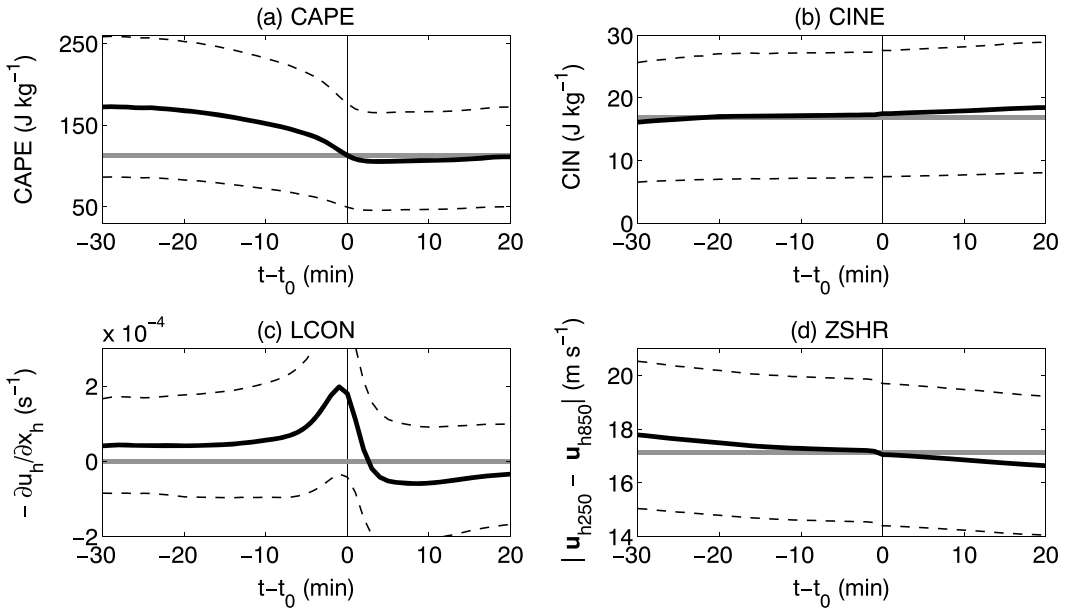

Figure 3. Time series of the following parameters at the grid point when convection was first detected, before and after the initiation of convection: (a) CAPE, (b) CIN, (c) low-level convergence (LCON), and (d) vertical shear of horizontal wind (ZSHR). The divergence is vertically averaged in the lowest 500 m. The vertical shear is defined as $\sqrt{\left(u_{\mathrm{bg},10.0}-u_{\mathrm{bg},1.5}\right)^2+\left(v_{\mathrm{bg},10.0}-v_{\mathrm{bg},1.5}\right)^2}$ where the subscript bg indicates the 100 km mean around the convection and is calculated between the 1.5 and 10.0 km altitudes. The thick black and gray lines indicate the averages at the convection-formed grid points and within the 100 km radius, respectively. The dashed line represents a quarter of the standard deviation.

We show the temporal variations of selected physical quantities that have been reported to play important roles in driving the convection at the grid points *where each convection event is first detected in its life cycle*. Figure 3 represents the time series of the following quantities: the CAPE, the low-level mass convergence, the convection inhibition (CIN), and the vertical wind shear at the convection-formed grid points before and after convection was initially detected. The CAPE calculated from the air parcel averaged in the lowest 500 m is larger than the surrounding mean and decreases until the convection initiation (i.e., $t = t_0$) (Figure 3a). Note that the surrounding mean is calculated inside the 100 km radius of the convection. The CIN that was calculated in the same way as CAPE keeps almost a constant value corresponding to the surrounding mean. The mass convergence averaged below the 500 m altitude rapidly decreases about 5–6 min prior to the initiation (Figure 3c). The vertical shear was defined as the wind difference between the 1.5 km and 10.0 km altitudes. Similar to the CIN, the vertical shear has little changes within the 50 min period with a slightly decreasing trend with time (Figure 3d).

In order to clearly see the relative importances of the four parameters, the temporal changes in the normalized parameters are shown in Figure 4. We calculated each parameter in the following manner: First, the averages and variances of the time series were calculated for each sample; the time series were then normalized by the averages and variances; and, finally, the normalized time series of all samples were composited. The deviations of CAPE and convergence from the environment before the initiation of moist convection were statistically significant satisfying the 99% confidence level by conducting the *t* test at each time (every 1 min). In contrast to these quantities, neither the CIN nor the vertical wind shear showed a clear difference from the environmental mean. We conducted the same analysis for other quantities such as the low-level temperature deviation from the environment and found that only these two quantities showed a clear signal before the initiation of moist convection. In short, convection on the global scale generally forms due to an enhanced low-level convergence in the presence of a high-CAPE environment.

The question now arises: what are the differences in convection and its precursors between the dynamically favorable (boundary layer convergence) and thermodynamically favorable (high-CAPE) conditions? Figure 5a shows a scatterplot of all the convection samples in an area of convergence and CAPE (convergence-CAPE

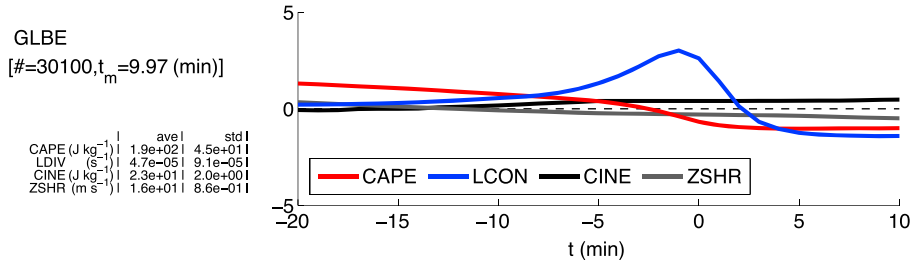

Figure 4. Time series of the normalized four parameters in Figure 3, which were obtained by first normalizing the quantities of each sample by the average and variance of the time series and then taking an average of all samples. The averages and standard deviations of quantities are listed in the figure. The red, blue, black, and gray lines stand for CAPE, low-level convergence (LCON), CIN, and vertical wind shear (ZSHR), respectively. The thin dashed line indicates the zero value. The total number of samples is 30,100, and the averaged time when the vertical maximum velocity of a convective cell reaches (t_m) is 9.97 min after the initial detection.

space). We divided them into four groups using thresholds, beyond which the sample number was 10% of the total (90th percentile). In the first group both exceeded the thresholds (marked with D); in the second group CAPE satisfied the top 10% condition, but convergence did not (C); in the third group convergence satisfied the top 10% condition, but CAPE did not (B); and in the fourth group neither satisfied the threshold (A).

Figures 5b–5e show the structure and temporal change in precursors of the convection in groups B and C. The convection structures were clearly different in the two groups, whereas the temporal overall evolution of the structure in both groups was qualitatively similar to that of the global average (figure not shown). In particular, the vertical velocity was stronger and the water content was higher in the high-CAPE group (C) than in the strong-convergence group (B) and the global average (Figures 5b and 5c). Thus, convection grew to reach a stronger intensity and higher altitude under the higher-CAPE environment, despite the fact that the time at which the vertical velocity reached its lifetime maximum did not differ significantly. The differences in maximum velocity and its altitude were statistically significant at the 95% confidence level. In contrast, in the strong-convergence group (B), the convergence started deviating from the average earlier than from the high-CAPE group (C) and global average (about 15 min).

In conclusion, the convection could obtain a strong intensity when CAPE was high before its initiation, whereas it was not as intense under the strong-convergence condition. The strong-convergence case produced a signal 15 min before the initiation of convection. In other words, the strength of convergence changes the time when the convergence departs from the environmental average. It suggests that the predictability time scale of convection is related to the strength of low-level convergence, whereas CAPE does not produce significant changes in the time scale; rather, it changes the strength of convection.

Figure 6 depicts the horizontal and latitudinal distributions of the difference in the number density of convection between the two groups. Convection in the high-CAPE group mainly occurred in the tropics as expected (red squares, Figure 6a). However, the samples in the strong-convergence group were not solely concentrated in the tropics but were also found in the midlatitudes, where convection was accompanied by midlatitudinal systems such as fronts [*Miyamoto et al.*, 2015]. At a given latitude, there was a large variety in the dominant precursors, especially in the Indian Ocean and in the western North Pacific (Figure 6a). In contrast, central Africa and the western part of South America were dominated by a single group. The convective cells in the former could be categorized as the high-CAPE group, whereas those in the latter were mainly in the strong-convergence group. The diversity among the continents may be due to the time difference: since the analyzed time was 00UTC, Africa is in the afternoon whereas North and South America are in the early morning. It should be noted that the present results are obtained from a 1 h integration and hence longer integrations are necessary to more comprehensively discuss the areal variations.

4. Concluding Remarks

A global simulation with very high spatiotemporal resolution, the grid spacing of 870 m and output interval of 1 min, was conducted using a nonhydrostatic global model (NICAM) with one of the world's fastest supercomputers (K computer). We developed a simple methodology detecting the deep convection core grid

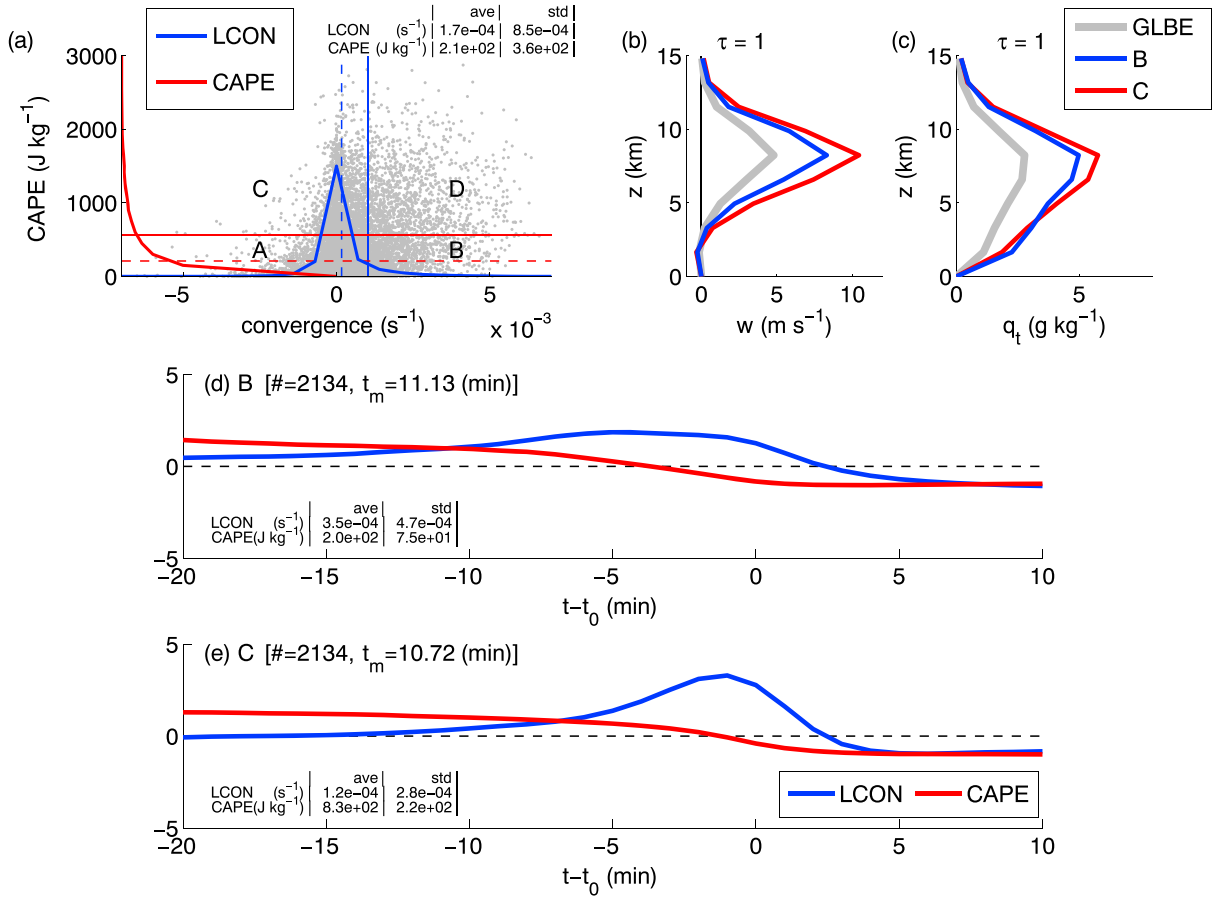

Figure 5. (a) Scatterplot of all the convection samples in the convergence-CAPE space. The thick lines indicate the normalized frequency. The thin dashed and solid lines are the average and average plus one standard deviation, respectively. The blue and red lines indicate the convergence and CAPE, respectively. The groups, A, B, C, and D, are defined in the text. (b) The vertical profile of vertical velocity for groups B (blue) and C (red) when the vertical velocity reaches its lifetime maximum ($\tau = 1$). (c) Same as Figure 5b but for the hydrometeor mixing ratio. (d, e) Same as Figure 4, but for group B (Figure 5d) and group C (Figure 5e) and showing only the low-level convergence and CAPE.

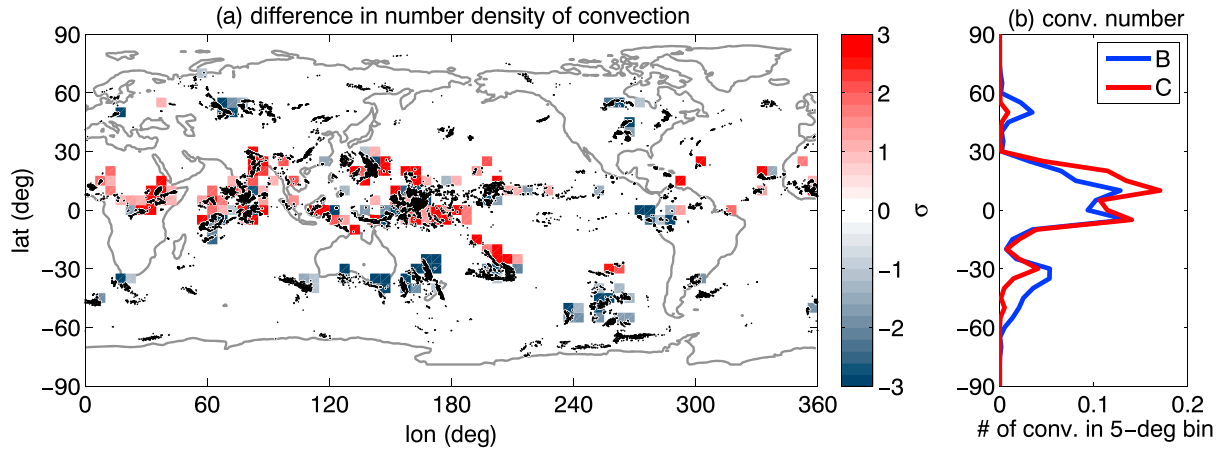

Figure 6. (a) Global view of the difference in number density of convection samples from the high-CAPE group (C) to the strong-convergence group (B). The dots represent the location of all the convection samples. The unit of color label is the standard deviation of the difference in number density (σ). (b) Latitudinal profiles of the number densities in the strong-convergence (blue) and the high-CAPE groups (red). The number densities were estimated in a 5 × 5° area and normalized by the total number of each group.

points and life cycle from a spatiotemporary discretized data. Since the method requires less thresholds, it can be utilized for the global data. Applying the developed method to the high-resolution global simulation output, 30,000 convection samples were approximately detected. The composites of temporal evolution of maximum vertical velocity and vertically averaged mixing ratio of hydrometeors, and radius-height cross section of convection samples were reasonable compared with observations of the convective cell (isolated thunderstorm [e.g., *Byers and Braham*, 1948a]).

We analyzed the obtained convection samples to examine the temporal change in several parameters related to the deep convection at the grid point where the convection cell was initially detected before and after the initiation of convection. The results presented here indicate that the parameters that act as precursors were amplified before the initiation of deep moist convection. In particular, the mass convergence in the boundary layer was amplified several minutes before the convection initiation and CAPE kept larger values than the surrounding mean (inside the 100 km distance from the convection core) until the initiation. The convection samples were divided into the four groups according to the magnitudes of low-level convergence and CAPE. We found that the low-level convergence deviated from the surrounding mean earlier in the group with strong convergence than that in all samples. The samples in the high-CAPE group obtained stronger maximum vertical velocity. Thus, it strongly suggests that the predictability time scale of convection depended on the magnitude of low-level convergence, whereas CAPE was a key function that determined the strength of convection and it was not directly related to the predictability of convection.

It is also shown that the dominant parameters were different from region to region on the globe. In the region where the convection was active in the present simulation [*Miyamoto et al*., 2015], we observed a large variety of the dominant parameter. In contrast, a single parameter dominated the continents (e.g., Africa or South America). This may be related to the time difference among the continents. Furthermore, it is suggested that the dominant precursor parameter is possibly different between the convection formed on the ocean and land. Hence, longer integrations are desired for more comprehensive discussions. Particularly, a daylong integration for diurnal cycle and a yearlong integration for seasonal cycle are desired for future works.

Acknowledgments

The authors thank three anonymous reviewers for their helpful comments, and H. Seko, S. Iga, S. Nishizawa, Y. Sato, S. Adachi, H. Miura, M. Satoh, S. Otsuka, K. Saito, T. Kawabata, Wei-Ting Chen, Chien-Ming Wu, and our colleagues for fruitful discussions. The simulations were performed using the K computer at the RIKEN Advanced Institute for Computer Science. The data are stored in a storage server at RIKEN, and it is available on request (ymiyamoto@riken.jp). Figure 1 was drawn using software developed by NCAR, VAPOR (www.vapor.ucar.edu).

References

Barthlott, C., et al. (2011), Initiation of deep convection at marginal instability in an ensemble of mesoscale models: A case-study from COPS, edited by V. Wulfmeyer, C. Flamant, A. Behrendt, A. Blyth, A. Brown, M. Dorninger, A. Illingworth, P. Mascart, A. Montani, and T. Weckwerth, *Q. J. R. Meteorol. Soc.*, *137*(S1), 118–136, doi:10.1002/qj.707.

Barthlott, C., J. W. Schipper, N. Kalthoff, B. Adler, C. Kottmeier, A. Blyth, and S. Mobbs (2010), Model representation of boundary-layer convergence triggering deep convection over complex terrain: A case study from COPS, *Atmos. Res.*, *95*(S1), 172–185, doi:10.1016/j.atmosres.2009.09.010.

Behrendt, A., et al. (2011), Observation of convection initiation processes with a suite of state-of-the-art research instruments during COPS IOP 8b, edited by V. Wulfmeyer, C. Flamant, A. Behrendt, A. Blyth, A. Brown, M. Dorninger, A. Illingworth, P. Mascart, A. Montani, and T. Weckwerth, *Q. J. R. Meteorol. Soc.*, *137*(S1), 81–100, doi:10.1002/qj.758.

Birch, C. E., J. H. Marsham, and D. J. Parker (2014), The scale dependence and structure of convergence fields preceding the initiation of deep convection, *Geophys. Res. Lett.*, *41*, doi:10.1002/(ISSN)1944-8007.

Bony, S., et al. (2015), Clouds, circulation and climate sensitivity, *Nature. Pub. Grp.*, *8*(4), 261–268, doi:10.1038/ngeo2398.

Byers, H. R., and R. R. Braham Jr. (1948a), Thunderstorm structure and circulation, *J. Meteor.*, *5*(3), 71–86, doi:10.1175/1520-0469(1948)005<0071:TSAC>2.0.CO;2.

Byers, H. R., and R. R. Braham Jr. (1948b), Thunderstorm structure and circulation, *J. Meteor.*, *5*(3), 71–86, doi:10.1175/1520-0469(1948)005<0071:TSAC>2.0.CO;2.

Ching, J., and A. J. Alkezweeny (1986), Tracer study of vertical exchange by cumulus clouds, *J. Clim. Appl. Meteorol.*, *25*(11), 1702–1711, doi:10.1175/1520-0450(1986)025<1702:TSOVEB>2.0.CO;2.

Doswell, C. A., III (1985), Storm scale analysis. Vol. II, The operational meteorology of convective weather.

Emanuel, K. A. (1994), *Atmospheric Convection*, Oxford University Press.

Hohenegger, C., and C. Schär (2007a), Atmospheric predictability at Synoptic Versus Cloud-Resolving Scales, *Bull. Amer. Meteor. Soc.*, *88*, 1783–1793, doi:10.1175/BAMS-88-11-1783.

Hohenegger, C., and C. Schär (2007b), Predictability and error growth dynamics in cloud-resolving models, *J. Atmos. Sci.*, *64*, 4467–4478, doi:10.1175/2007JAS2143.1.

Houze, R. A., Jr. (1994), *Cloud Dynamics*, Academic Press.

Jorgensen, D. P., and M. A. LeMone (1989), Vertical velocity characteristics of oceanic convection, *J. Atmos. Sci.*, *46*(5), 621–640, doi:10.1175/1520-0469(1989)046<0621:VVCOOC>2.0.CO;2.

Jorgensen, D. P., and T. M. Weckwerth (2003), Forcing and organization of convective systems, *Meteor. Monogr.*, doi:10.1175/0065-9401(2003)030<0075:FAOOCS>2.0.CO;2.

Kajikawa Y., Y. Miyamoto, R. Yoshida, T. Yamaura, H. Yashiro, and H. Tomita (2016), Resolution dependence of deep convections in a global simulation from over 10-kilometer to sub-kilometer grid spacing, *Prog. Earth Planet. Sci.*, doi:10.1186/s40645-016-0094-5. (in press)

Kalnay, E., M. Kanamitsu, R. Kistler, W. Collins, D. Deaven, L. Gandin, M. Iredell, and S. Saha (1996), The NCEP/NCAR 40-year reanalysis project, *Bull. Amer. Meteor. Soc.*, *77*(3), 437–471, doi:10.1175/1520-0477(1996)077<0437:TNYRP>2.0.CO;2.

Kalthoff, N., et al. (2009), The impact of convergence zones on the initiation of deep convection: A case study from COPS, *Atmospheric Research*, *93*, 680–694, doi:10.1016/j.atmosres.2009.02.010.
Leinonen, J., M. D. Lebsock, S. Tanelli, K. Suzuki, H. Yashiro, and Y. Miyamoto (2015), Performance assessment of a triple-frequency spaceborne cloud–precipitation radar concept using a global cloud-resolving model, *Atmos. Meas. Tech.*, *8*(8), 3493–3517, doi:10.5194/amt-8-3493-2015.
LeMone, M. A., and E. J. Zipser (1980), Cumulonimbus vertical velocity events in GATE. Part I: Diameter, intensity and mass flux, *J. Atmos. Sci.*, *37*(11), 2444–2457, doi:10.1175/1520-0469(1980)037<2444:CVVEIG>2.0.CO;2.
Lorenz, E. N. (1969), The predictability of a flow which possesses many scales of motion, *Tellus*, doi:10.1111/j.2153-3490.1969.tb00444.x.
Louis, J.-F. (1979), A parametric model of vertical eddy fluxes in the atmosphere, *Boundary-Layer Meteorol*, *17*(2), 187–202, doi:10.1007/BF00117978.
Mapes, B., R. Milliff, and J. Morzel (2009), Composite life cycle of maritime tropical mesoscale convective systems in scatterometer and microwave satellite observations, *J. Atmos. Sci.*, *66*, 199–208, doi:10.1175/2008JAS2746.1.
Masunaga, H. (2014), Free-tropospheric moisture convergence and tropical convective regimes, *Geophys. Res. Lett.*, doi:10.1002/(ISSN)1944-8007.
Masunaga, H., and T. S. L'Ecuyer (2014), A mechanism of tropical convection inferred from observed variability in the moist static energy budget, *J. Atmos. Sci.*, *71*(10), 3747–3766, doi:10.1175/JAS-D-14-0015.1.
Melhauser, C., and F. Zhang (2012), Practical and intrinsic predictability of severe and convective weather at the mesoscales, *J. Atmos. Sci.*, *69*, 3350–3371, doi:10.1175/JAS-D-11-0315.1.
Miyamoto, Y., R. Yoshida, T. Yamaura, H. Yashiro, H. Tomita, and Y. Kajikawa (2015), Does convection vary in different cloud disturbances?, *Atmos. Sci. Lett.*, doi:10.1002/asl2.558.
Miyamoto, Y., Y. Kajikawa, R. Yoshida, T. Yamaura, H. Yashiro, and H. Tomita (2013), Deep moist atmospheric convection in a subkilometer global simulation, *Geophys. Res. Lett.*, doi:10.1002/grl.50944.
Nakanishi, M., and H. Niino (2004), An improved Mellor–Yamada level-3 model with condensation physics: Its design and verification, *Boundary-Layer Meteorol*, *112*, 1–31, doi:10.1023/B:BOUN.0000020164.04146.98.
Nasuno, T., and M. Satoh (2011), Properties of precipitation and in-cloud vertical motion in a global nonhydrostatic aquaplanet experiment, *JMSJ*, doi:10.2151/jmsj.2011-502.
Noda, A. T., K. Oouchi, M. Satoh, H. Tomita, and S. Iga (2010), Importance of the subgrid-scale turbulent moist process: Cloud distribution in global cloud-resolving simulations, *Atmos. Res.*, doi:10.1016/j.atmosres.2009.05.007.
Petch, J. C. (2004), The predictability of deep convection in cloud-resolving simulations over land, *Q. J. R. Meteorol. Soc.*, *130*, 3173–3187, doi:10.1256/qj.03.107.
Plant, R. S. (2009), Statistical properties of cloud lifecycles in cloud-resolving models, *Atmos. Chem. Phys.*, *9*, 2195–2205, doi:10.5194/acp-9-2195-2009.
Rossow, W. B., and R. A. Schiffer (1999), Advances in understanding clouds from ISCCP, *Bull. Am.*, doi:10.1175/1520-0477(1999)080<2261:AIUCFI>2.0.CO;2.
Satoh, M., et al. (2014), The non-hydrostatic icosahedral atmospheric model: Description and development, *Prog. Earth Planet. Sci.*, *1*(1), 18, doi:10.1186/s40645-014-0018-1.
Satoh, M., T. Matsuno, H. Tomita, H. Miura, T. Nasuno, and S. Iga (2008), Nonhydrostatic icosahedral atmospheric model (NICAM) for global cloud resolving simulations, *J. Comput. Phys.*, *227*, 3486–3514, doi:10.1016/j.jcp.2007.02.006.
Sekiguchi, M., and T. Nakajima (2009), The improvement of the absorption process using a computational optimization in an atmospheric general circulation model, Current Problems in Atmospheric Radiation, doi:10.1063/1.3117081.
Sherwood, S. C., and R. Wahrlich (1999), Observed evolution of tropical deep convective events and their environment, *Mon. Wea. Rev.*, *127*, 1777–1795.
Stevens, B., and S. Bony (2013), What are climate models missing?, *Science*, *340*(6136), 1053–1054, doi:10.1126/science.1237554.
Takemi, T. (2008), An eddy-resolving simulation of the diurnal variation of fair-weather convection and tracer transport, *Atmos. Res.*, *89*, 270–282, doi:10.1016/j.atmosres.2008.02.012.
Tomita, H. (2008), New microphysical schemes with five and six categories by diagnostic generation of cloud ice, *J. Meteor. Soc. Jpn. Ser II*, *86A*, 121–142, doi:10.2151/jmsj.86A.121.
Tomita, H., and M. Satoh (2004), A new dynamical framework of nonhydrostatic global model using the icosahedral grid, *Fluid Dyn. Res.*, *34*, 357–400, doi:10.1016/j.fluiddyn.2004.03.003.
Weckwerth, T. M., and D. B. Parsons (2006), A review of convection initiation and motivation for IHOP_2002, *Mon. Wea. Rev.*, *134*, 5–22, doi:10.1175/MWR3067.1.
Wulfmeyer, V., et al. (2008), The convective and orographically induced precipitation study: A research and development project of the World Weather Research Program for improving quantitative precipitation forecasting in low mountain regions, *Bull. Amer. Meteor. Soc.*, *89*, 1477–1486, doi:10.1175/2008BAMS2367.1.
Wulfmeyer, V., et al. (2011), The Convective and Orographically induced Precipitation Study (COPS): The scientific strategy, the field phase, and research highlights, *Q. J. R. Meteorol. Soc.*, *137*, 3–30, doi:10.1002/qj.752.
Zhang, F., C. Snyder, and R. Rotunno (2003), Effects of moist convection on mesoscale predictability, *J. Atmos. Sci.*, *60*(9), 1173–1185, doi:10.1175/1520-0469(2003)060<1173:EOMCOM>2.0.CO;2.
Zhang, F., N. Bei, R. Rotunno, C. Snyder, and C. C. Epifanio (2007), Mesoscale predictability of moist baroclinic waves: Convection-permitting experiments and multistage error growth dynamics, *J. Atmos. Sci.*, *64*, 3579–3594, doi:10.1175/JAS4028.1.